1 **Low-Cost, High-Precision, Single-Frequency GPS-BDS RTK Positioning**

2 Robert Odolinski[1], Peter J. G. Teunissen[2,3]

3

4 **Abstract** The integration of the Chinese BDS with other systems, such as the American GPS,

5 makes precise RTK positioning possible with low-cost receivers. We investigate the performance

6 of low-cost ublox receivers, which cost a few hundred USDs, while making use of L1 GPS + B1

7 BDS data in Dunedin, New Zealand. Comparisons will be made to L1 + L2 GPS and survey-grade

8 receivers which cost several thousand USDs. The least-squares variance component estimation

9 (LS-VCE) procedure is used to determine the code and phase variances and covariances of the

10 receivers and thus formulate a realistic stochastic model. Otherwise the ambiguity resolution and

11 hence positioning performance would deteriorate. For the same reasons, the existence of receiver-

12 induced time-correlation is also investigated. The low-cost RTK performance is then evaluated by

13 formal and empirical ambiguity success-rates and positioning precisions. It will be shown that the

14 code and phase precision of the low-cost receivers can be significantly improved by using survey-

15 grade antennas, since they have better signal reception and multipath suppression abilities in

16 comparison to low-cost patch antennas. It will also be demonstrated that the low-cost receivers can

17 achieve competitive ambiguity resolution and positioning performance to survey-grade dual-

18 frequency GPS receivers.

19 *Keywords* Low-cost Receiver, Multi-GNSS, Real Time Kinematic (RTK) positioning, Least-

20 squares variance component estimation (LS-VCE), Time-correlation

21

22 **Introduction**

23 In the past few decades, the American Global Positioning System (GPS) has been the primary

24 positioning tool for many applications. The integration with the emerging Global Navigation

25 Satellite Systems (GNSSs), such as the Chinese BeiDou Navigation Satellite System (BDS), can

[1] National School of Surveying, University of Otago, 310 Castle Street, 9016 Dunedin, New Zealand, email: robert.odolinski@otago.ac.nz

[2] Department of Spatial Sciences, GNSS Research Centre, Curtin University, Perth, Australia

[3] Delft University of Technology, Delft, The Netherlands

give improved precise real-time kinematic (RTK) positioning. Some first results using BDS outside of China are reported in Montenbruck et al. (2013) and Nadarajah et al. (2013). When BDS is combined with GPS about double the number of satellites will be visible in the Asia-pacific region, which can make single-frequency RTK (Verhagen et al. 2012; He et al. 2014; Teunissen et al. 2014; Odolinski et al. 2015) and low-cost receiver RTK positioning possible (Odolinski and Teunissen 2016; Mongredien et al. 2016). Other studies on GPS RTK positioning and ambiguity resolution using low-cost receivers can be found in Takasu and Yasuda (2008;2009), Wisniewski et al. (2013) and Pesyna et al. (2014). We will analyze the performance of L1 GPS + B1 BDS in Dunedin, New Zealand using low-cost ublox receivers. We will compare the performance to that of dual-frequency GPS survey-grade receivers.

We describe first the GPS+BDS functional/stochastic model, and then the real data used for our evaluations. Least-squares variance component estimation (LS-VCE) results are then presented as a way to determine the code and phase (co)variances and formulate a realistic stochastic model. An incorrect stochastic model deteriorates the ambiguity resolution performance and consequently impacts the achievable positioning precisions. For that same reasons, receiver-induced time-correlation will also be investigated. Once the stochastic model has been correctly defined, the ambiguity resolution and positioning performance is investigated. The performance is evaluated formally and empirically, for customary and high elevation cut-off angles. The high cut-off angles are used to mimic situations when low-elevation multipath is to be avoided. All results will be compared between using low-cost and survey-grade antennas. We then further extend our short-baseline analysis and investigate the performance for a baseline where small residual ionospheric delays are present. A summary with conclusions is finally given.

GPS+BDS model

The model that will be used for the LS-VCE, as introduced in Teunissen (1988), is given as follows. Assume that $s_G + 1$ GPS satellites are tracked on f_G frequencies and $s_B + 1$ BDS satellites on f_B frequencies. As we apply system-specific double-differencing (DD) one pivot satellite is used per system. The total number of DD phase and code observations per epoch equals then $2f_G s_G + 2f_B s_B$. We assume for now that cross-correlation between frequencies, and code and phase is absent. Following Teunissen et al. (2014), the combined multi-frequency short-

56   baseline GPS+BDS model is then defined as follows.

57   The system-specific DD phase and code observation vectors are denoted as ϕ_* and p_*,

58   respectively, with $*= \{G, B\}$ where $G =$ GPS and $B =$ BDS. The single-epoch GNSS model of

59   the combined system is given as

60
$$\begin{bmatrix} \phi \\ p \end{bmatrix} - \begin{bmatrix} \Lambda & I \\ 0 & I \end{bmatrix} \begin{bmatrix} a \\ \rho \end{bmatrix} = \begin{bmatrix} \varepsilon \\ e \end{bmatrix} \tag{1}$$

61   and

62
$$D \begin{bmatrix} \phi \\ p \end{bmatrix} = \begin{bmatrix} Q_{\phi\phi} & 0 \\ 0 & Q_{pp} \end{bmatrix} \tag{2}$$

63   in which $\phi = [\phi_G^T, \phi_B^T]^T \in \mathbb{R}^{f_G s_G + f_B s_B}$ is the combined phase vector, $p = [p_G^T, p_B^T]^T \in$

64   $\mathbb{R}^{f_G s_G + f_B s_B}$ the combined code vector, $a = [a_G^T, a_B^T]^T \in \mathbb{Z}^{f_G s_G + f_B s_B}$ the combined integer

65   ambiguity vector, $\rho = [\rho_G^T, \rho_B^T]^T \in \mathbb{R}^{s_G + s_B}$ the receiver-satellite range, $\varepsilon = [\varepsilon_G^T, \varepsilon_B^T]^T \in$

66   $\mathbb{R}^{f_G s_G + f_B s_B}$ the combined phase random observation noise vector, $e = [e_G^T, e_B^T]^T \in \mathbb{R}^{f_G s_G + f_B s_B}$

67   the combined code random observation noise vector, $D[.]$ denotes the dispersion operator, and

68   with the entries of the wavelength matrix given as

69   $\Lambda = \text{blkdiag}[\Lambda_G, \Lambda_B], \quad \Lambda_* = \text{diag}[\lambda_{1_*}, \dots, \lambda_{f_*}] \otimes I_{s_*}$

70   where λ_{j_*} is the wavelength of frequency j_*, $\otimes$ denotes the Kronecker product, I_{s_*} is the

71   $s_* \times s_*$ unit matrix, 'diag' is a diagonal and 'blkdiag' a blockdiagonal matrix, respectively. The

72   entries of the positive definite variance matrices are given as

73
$$\begin{aligned}
&Q_{\phi\phi} = \text{blkdiag}[Q_{\phi_G \phi_G}, Q_{\phi_B \phi_B}], Q_{\phi_* \phi_*} = C_{\phi_* \phi_*} \otimes 2Q_* \\
&Q_{pp} = \text{blkdiag}[Q_{p_G p_G}, Q_{p_B p_B}], Q_{p_* p_*} = C_{p_* p_*} \otimes 2Q_* \\
&C_{\phi_* \phi_*} = \text{diag}[\sigma_{\phi_{1_*}}^2, \dots, \sigma_{\phi_{f_*}}^2], C_{p_* p_*} = \text{diag}[\sigma_{p_{1_*}}^2, \dots, \sigma_{p_{f_*}}^2] \\
&Q_* = D_{s_*}^T W_*^{-1} D_{s_*}, W_* = \text{diag}[w_{1_*}, \dots, w_{s_*+1}]
\end{aligned} \tag{3}$$

74   where $D_{s_*}^T = [-e_{s_*}, I_{s_*}]$ is the $s_* \times (s_* + 1)$ differencing matrix, e_{s_*} is the $s_* \times 1$ vector of

75   values of 1, $\sigma_{\phi_{j_*}}$, $\sigma_{p_{j_*}}$ the phase and code standard deviation, respectively, and w_{i_*} denotes the

76   satellite elevation dependent weight.

77   The model (1) applies to short baselines, and thus the ionospheric and tropospheric delays

78   are assumed absent. The broadcast ephemerides are used to obtain the satellite coordinates and the

79   baseline is precisely known. Hence the receiver-satellite range ρ is known, which is referred to as

80   the "geometry-fixed" model. The Least-squares AMBiguity Decorrelation Adjustment
81   (LAMBDA) (Teunissen 1995) is furthermore used to estimate the integer ambiguities a and treat
82   them as time-constant parameters over a large observation time span, so that their uncertainty can
83   be assumed to be negligible, which is referred to as the "ambiguity-fixed" model. The observation
84   noise vectors ε and e, respectively, are zero-mean vectors provided that no multipath is present
85   in (1).

86

87   **Experiment setup**

88   The GNSS receivers used to collect GNSS data are depicted in Figure 1. Two ublox EVK-M8T
89   receivers were setup to collect L1+B1 GPS+BDS data for two days with a measurement interval
90   of 1 s. These low-cost receivers cost a few hundred USDs. Since patch antennas have been shown
91   to have less effective signal reception and multipath suppression in comparison to survey-grade
92   antennas (Pesyna et al. 2014), the receivers that collected data for two days were also connected
93   to Trimble Zephyr 2 antennas. These antennas have a cost of slightly more than one thousand
94   USDs per antenna. To compare the low-cost solution to a survey-grade solution, two Trimble
95   NetRS receivers, which cost several thousand USDs, were connected to the same Zephyr antennas
96   through a splitter and collected L1+L2 GPS data. Another receiver setup, with Zephyr antennas,
97   was also analyzed with a baseline length of 7 km, so as to evaluate the low-cost receiver
98   performance when small residual ionospheric delays are present. The detection, identification, and
99   adaption (DIA) procedure (Teunissen 1990) was furthermore used to eliminate any outliers.
100   The model we will use for positioning is obtained by linearizing the observation equations
101   in (1) with respect to the unknown receiver coordinates. Figure 2 depicts the corresponding
102   redundancy of the two models when also including ambiguities as unknown parameters, together
103   with the number of satellites over 48 h with a 30 s epoch interval.
104

105
106 **Fig. 1** GNSS ublox EVK-M8T receivers collecting data for GPS + BDS single-baseline RTK, with

107 patch antennas (top, left) and Trimble Zephyr 2 antennas (top, right) in Jan 4-6 and Jan 6-8, 2016,

108 respectively. Survey-grade Trimble NetRS dual-frequency GPS receivers have been connected to

109 the same Zephyr 2 antennas to truly track the same GPS constellation. A 7 km baseline setup (Jan

110 18-19, 2016) also used to assess the positioning performance is shown at bottom

111
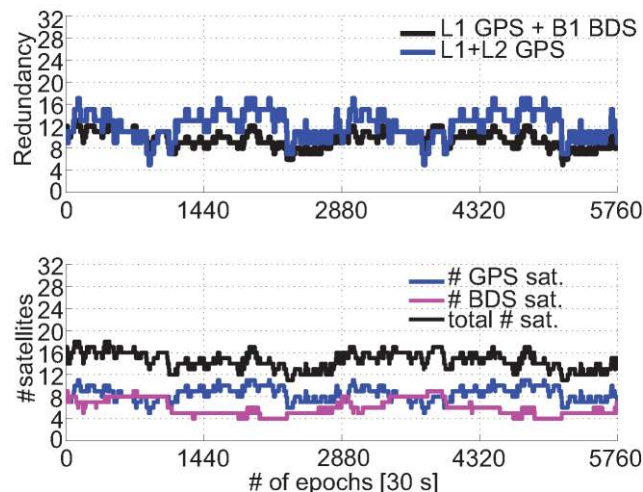
112
113 **Fig.   2** Number (#) of satellites (bottom) and redundancy (top) of L1+B1 GPS+BDS and L1+L2

114 GPS in Jan 6-8, 2016 (48 h) for an elevation cut-off angle of 10°

115

116   While the number of BDS satellites (magenta lines) is overall smaller than when compared

117 to GPS (blue lines) in Dunedin, Figure 2 shows that the redundancy of L1+B1 GPS+BDS is almost

118 similar to that of L1+L2 GPS except for some hours at the middle of the two days. This implies,

119 for instance, that the two models can potentially give competitive RTK ambiguity resolution and

120 positioning performance, see the extensive overviews in Teunissen et al. (2014) and Odolinski and

121 Teunissen (2016). This is however only true if the receiver-satellite geometry strength and receiver

122 code and phase observation noise would be of similar magnitude between the receivers used, hence

123 the need for an analysis of the observation precision.

124   In the following receiver evaluations, a set of reference ambiguities were determined using

125 a known baseline and treated as time-constant parameters over the two days in a dynamic model.

126 Note also that the Geostationary Orbit (GEO) C03 BDS satellite had to be excluded from all the

127 results as it yielded many incorrectly fixed instances caused by low-elevation multipath (Wang et

128 al. 2015a; 2015b), due to it being almost stationary and having a low elevation angle of around

129 12° with respect to the receivers (Odolinski and Teunissen 2016).

130

Least-squares Variance Component Estimation for low-cost receivers

132 We make use of the LS-VCE procedure (Teunissen 1988; Teunissen and Amiri-Simkooei 2008)

133 to determine the code and phase precision of the low-cost receivers. The estimated (co)variances

134 are needed to formulate a realistic stochastic model for precise RTK positioning. The ambiguity

135 resolution performance would otherwise deteriorate and hence the achievable positioning

136 precisions as well.

137   The noise vectors for phase ε and code e in (1) serve as an input into the LS-VCE. To

138 capture the elevation dependency, an exponential weighting function (Euler and Goad 1991) is

139 used in (3) as follows

140 $$w_{i_*} = \left[1 + 10\exp\left(-\frac{\theta^{i_*}}{10}\right)\right]^{-2} \tag{4}$$

141 where θ^{i_*} is the elevation of the satellite i_* in degrees. This formulation allows us to estimate

142 zenith-referenced standard deviations (STDs) of the undifferenced phase and code observations,

143 $\sigma_{\phi_{j_*}}$ and $\sigma_{p_{j_*}}$, respectively. Table 1 depicts the corresponding code and phase STDs for the short-

144 baseline setups at top of Figure 1 for instantaneous, i.e. epoch-by-epoch, RTK. The presented

145 STDs are the mean of the single-epoch STDs over the entire observation time span. The STDs

146 within parentheses are based on single-epoch multipath (MP) corrected DD residuals. These

147 residuals were obtained by subtracting the DD residuals (1) from the previous day of data (Jan 6

148 minus Jan 5 for patch and Jan 9 minus Jan 8 for Zephyr antennas), while taking into account the

149 approximate satellite constellation repeatability of 23 h and 56 min and using the elevation

150 weighting (4) similar to Zaminpardaz et al. (2016). This procedure was applied since the code e

151 and phase ε vectors in (1) are believed to be contaminated by multipath effects. The MP correction

152 was only applied to the GPS Medium Earth Orbit (MEO) and BDS GEO/Inclined Geosynchronous

153 Satellite Orbit (IGSO), since these satellites have a constellation repeatability of about one sidereal

154 day (Axelrad et al. 2005; Jiang et al. 2011), and the GEO satellites are almost stationary

155 (Montenbruck et al. 2013). One should, however, also be aware of that different satellites can have

156 different repeatability periods that differ several seconds from each other, as was shown for GPS

157 (Axelrad et al. 2005). We use the same time-separation between days for all satellites when

158 applying the MP corrections, which consequently can result in some residual multipath effects to

159 remain in the presented results. The doubling in noise that enters through the epoch-by-epoch MP

160 correction has been accounted for in all the results presented by dividing the day-differenced

161 residuals by square root of two.

162

163 **Table 1** LS-VCE of zenith-referenced and undifferenced code $\hat{\sigma}_{p_{j_*}}$ and phase $\hat{\sigma}_{\phi_{j_*}}$ STDs for

164 Dunedin. The STDs based on MP-corrected DD residuals are shown within parentheses. The STDs

165 have been estimated based on models including all satellites unless otherwise stated, and always

166 including GPS. The 24 h (30 s) period is 22:00-22:00 (hh:mm) UTC Jan 4-5 for ublox+patch,

167 21:48-21:48 UTC Jan 7-8 for ublox/Trimble NetRS+Zephyr. The 2 h (1 s) period for GPS is 04:00-

168 06:00 UTC Jan 5 for patch and 03:48-05:48 UTC Jan 8 for Zephyr. The corresponding BDS STDs

169 are based on 18:00-20:00 UTC Jan 5 for patch and 17:48-19:48 UTC Jan 8, 2016 for Zephyr

Receiver/antenna	System	Frequency	2 h [1 s interval]		24 h [30 s interval]	
			$\hat{\sigma}_{p_{j_*}}$ [cm]	$\hat{\sigma}_{\phi_{j_*}}$ [mm]	$\hat{\sigma}_{p_{j_*}}$ [cm]	$\hat{\sigma}_{\phi_{j_*}}$ [mm]
Trimble NetRS	GPS	L1	18(15)	2(1)	18	2
+Zephyr		L2	20(15)	2(1)	20	2
ublox EVK-M8T	GPS	L1	31(20)	2(1)	34	2
+Zephyr	BDS	B1	30(−)	2(−)	29	2
	GEO + IGSO		33(20)	2(1)	29	2
ublox EVK-M8T	GPS	L1	53(24)	2(1)	49	2
+patch	BDS	B1	73(−)	2(−)	49	2
	GEO + IGSO		74(22)	2(1)	47	2

170

171   In support of understanding Table 1 better, Figure 3 shows the single-epoch B1 BDS code

172   and phase STDs (left two columns) corresponding to a period of two hours. The code and phase

173   DD residuals are also shown for two consecutive days (right two columns), where elevation-

174   weighting (4) is applied since the observations are highly dependent on the elevation of the

175   satellites. The patch-antenna residuals and corresponding single-epoch estimated STDs show very

176   large fluctuations at times likely due to multipath or poor signal reception since it repeats over

177   both days. The code and phase STDs based on elevation-weighted day-differenced DD residuals

178   are thus depicted as well at the second and fourth row respectively.

179
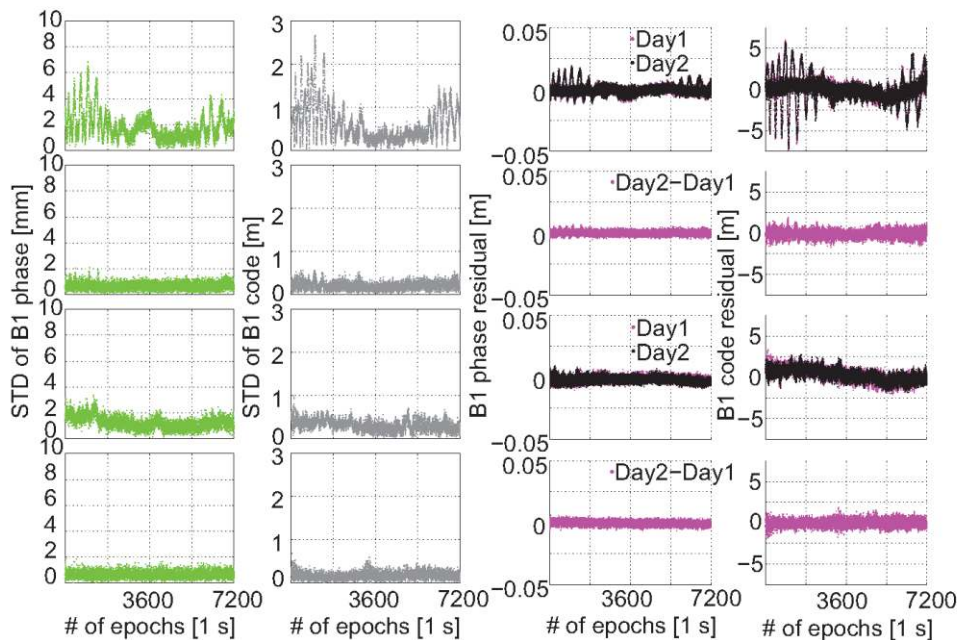
180
181

Fig. 3 Single-epoch LS-VCE of zenith-referenced and undifferenced B1 BDS code and phase
STDs (left two columns) for Day1 (2h [1 s]) using ublox EVK-M8T receivers and L1+B1
GPS+BDS. The elevation-weighted code/phase DD residuals are also shown (right two columns),
all in the first and third row. The corresponding STDs and code and phase DD residuals when
applying MP corrections are shown in the second and fourth row, using a repeatability period of
approximately one sidereal day for the GPS MEO and BDS GEO+IGSO satellites. In the first two
rows results are given for patch on Jan 5 at 18:00 and Jan 6 at 17:56 (hh:mm) UTC, and in the last
two rows when Zephyr antennas are used on Jan 8 at 17:48 and Jan 9, 2016 at 17:44 (hh:mm) UTC

190   Figure 3 shows the significant improved patch antenna STDs when the MP corrections
191 have been applied (second row left), which is also reflected by the corresponding much smaller
192 residuals (second row right). Table 1 shows consequently the more similar magnitude of STDs
193 between using Zephyr and patch antennas for the u-blox receivers when MP corrections have been
194 applied. For example, the B1 code STD decreases from 74 cm for the patch-antenna model to 22
195 cm when day-differencing has been applied. Corresponding values for the Zephyr-antenna model
196 are 33 cm, which decreases to 20 cm. Since the non-differenced STDs for the patch antenna
197 model are much larger than the corresponding Zephyr ones, this indicates the potentially better
198 multipath suppression by the Zephyr antennas which is also reflected by the much smaller code
199 and phase residuals in the figure. We also note in Table 1 that the Trimble NetRS non-differenced
200 L1 and L2 code STDs of 18 cm and 20 cm, respectively, decrease to 15 cm for both frequencies
201 when day-differencing has been applied.

202   The covariances between code and phase, and frequencies, were also estimated. Table 2
203 shows the corresponding cross-correlations together with the STDs based on the 2 h (1 s) data in
204 Table 1, whereas the patch-antenna model is based on 24 h (30 s) due to the earlier-referenced
205 possibility of multipath so that these effects are more likely to average out over time.

206

207 **Table 2** LS-VCE of zenith-referenced cross-correlations, which are the non-diagonal values, and
208 undifferenced code $\hat{\sigma}_{p_{j_*}}$ and phase $\hat{\sigma}_{\phi_{j_*}}$ STDs, which are the diagonal values. This is all given
209 for Dunedin on $j_* = 1_*, \ldots, f_*$. The estimation is based on 2 h of data (1 s) whereas the patch
210 antenna model is based on 24 h (30 s), while making use of the same periods as specified in
211 Table 1. The BDS values have been estimated based on using all GPS+BDS satellites

Receiver/antenna	System		C1C	L1C	C2W	L2W
Trimble NetRS	GPS	C1C	18 cm	0.1	0.1	
+Zephyr 2 h [1 s]		L1C	0.1	2 mm		0.35
		C2W	0.1		20 cm	-0.1
		L2W		0.35	-0.1	2 mm
			C1C	L1C	C2I	L2I
ublox EVK-M8T	GPS	C1C	31 cm	-0.1		
+Zephyr 2 h [1 s]		L1C	-0.1	2 mm		
	BDS	C2I			30 cm	0.0
		L2I			0.0	2 mm
			C1C	L1C	C2I	L2I
ublox EVK-M8T	GPS	C1C	49 cm	-0.1		
+patch 24 h [30 s]		L1C	-0.1	2 mm		
	BDS	C2I			49 cm	0.0
		L2I			0.0	2 mm

212

213   Table 2 shows that the Trimble NetRS receivers have an estimated correlation coefficient

214 of 0.35 between L1C and L2W phase, which is significant since the corresponding STD is 0.007

215 that is not explicitly shown herein. That the GPS L1 and L2 phase observables can be highly

216 correlated for some receivers has also been found in Teunissen et al. (1998), Bona and Tiberius

217 (2000), Amiri-Simkooei and Tiberius (2007), and Amiri-Simkooei et al. (2009), and specifically

218 for a Trimble NetRS receiver in Amiri-Simkooei et al. (2016). More importantly the ublox

219 receivers show close to zero cross-correlation between GPS C1C code and L1C phase, as well as

220 BDS C2I code and L2I phase.

221

Time-correlation of low-cost RTK positioning

223 In this section we examine the time-correlation of the low-cost receivers, which, if neglected in a

224 multi-epoch model, could negatively influence the ambiguity resolution and hence positioning

225 performance. Time-correlation can be caused by internal effects in the receivers, for instance

226 filtering to reduce the observation noise level (Bona 2000). External effects can also cause time-

227 correlation, which include atmospheric delays and multipath. We use a short-baseline (SB) setup

228 (Figure 1, top), and thus multipath is the main external source herein that can cause time-

229 correlation in addition to the internal effects within the receivers. We will also compare the results

230 to a zero-baseline (ZB) setup, where two receivers are connected to the same antenna at the same

231 location as the setups shown at the top of Figure 1. As a result of the zero-baseline set-up, the

232 contributions of multipath are largely eliminated. The remaining small effects would mainly be

233 due to the non-simultaneity of sampling between the receivers. One should finally be aware that

234 internal errors due to the noise from the common Low Noise Amplifier (LNA) between the

235 receivers largely extent cancel when a zero-baseline is used (Amiri-Simkooei and Tiberius 2007).

236 This is the reason that the receiver noise thus far has only been assessed based on the short baseline

237 setups in Figure 1, where the receivers are connected to their own antenna and LNA, and thus give

238 more realistic noise estimates.

239

Time-correlation without reducing multipath

241 The model we will now use is obtained by linearizing the observation equations in (1) with respect

242   to the unknown receiver coordinates. In this step, the code and phase variances that were estimated

243   by LS-VCE in Table 2 are fixed. We consider estimating a functionally known quantity, like local

244   North/East/Up ambiguity-float or ambiguity-fixed components respectively, and m is the number

245   of times. These positioning errors were obtained by comparing the estimated positions to precise

246   benchmark coordinates. The autocovariance function can then be determined by (Teunissen and

247   Amiri-Simkooei 2008)

248    $$\hat{\sigma}_\tau = \frac{\sum_{i=1}^{m-\tau} \hat{e}_i \hat{e}_{i+\tau}}{m-\tau}, \tau = 1,2,\dots,m-1 \tag{5}$$

249   where τ is the time-lag and $\hat{e}_i$ the least-squares positioning errors. The variance of the noise

250   process follows as,

251    $$\hat{\sigma}^2 = \frac{\sum_{i=1}^{m} \hat{e}_i \hat{e}_i}{m} \tag{6}$$

252   The autocorrelation function can then be defined by,

253    $$\hat{\rho}_\tau = \frac{\hat{\sigma}_\tau}{\hat{\sigma}^2}, \tau = 1,2,\dots,m-1 \tag{7}$$

254   where $\hat{\rho}_{\tau=0} = 1$ by definition. An approximation of the STD of the autocorrelation function is

255   given through linearization and the error propagation law of (7) as follows under the assumption

256   of white noise, i.e. that consecutive observations are uncorrelated (Amiri-Simkooei and Tiberius

257   2007),

258    $$\sigma_{\hat{\rho}_\tau} \approx \sqrt{\frac{1}{m-\tau} + \frac{2\hat{\rho}_\tau^2}{m}}, \tau = 1,2,\dots,m-1 \tag{8}$$

259   Equation (8) shows that with increasing time-lags τ the precision of the estimated time-correlation

260   (7) becomes poorer, which makes sense since the number of positions used to estimate the

261   autocovariance $\hat{\sigma}_\tau$ (5) is $m-\tau$. To see this at work, Figure 4 depicts the autocorrelation function

262   (7) in green for instantaneous ambiguity-fixed L1+B1 GPS+BDS RTK positioning for the local

263   Up-component. This is based on 1 h (1 s) of data for ublox+patch at top and ublox+Zephyr at

264   bottom for the short-baselines in Figure 1. In order to separate the contribution of multipath on the

265   time-correlation estimates we depict in black color the corresponding autocorrelation for a zero-

266   baseline ublox+patch antenna setup, which collects independent data with approximately the same

267   satellite configuration to the short-baselines but about 100 days later. This is given together with

268   the 95% confidence interval (CI) in red as computed from the STD of the autocorrelation in (8).

269
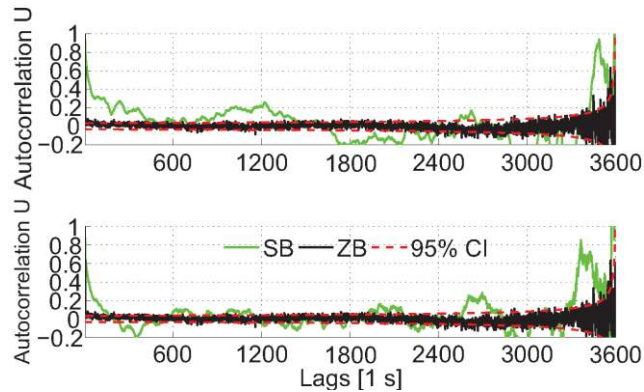
270
271 **Fig. 4** Autocorrelation coefficients (green) for L1+B1 GPS+BDS instantaneous short-baseline
272 ambiguity-fixed positioning errors during 1 h (1 s). The results are based on data on Jan 5 at
273 02:50 for ublox+patch at top and Jan 8, 2016 at 02:38 (hh:mm) UTC for ublox+Zephyr at bottom.
274 Autocorrelation coefficients are also depicted for a ublox+patch zero-baseline setup in black color,
275 on Apr 15, 2016 at 19:39 (hh:mm) UTC. Their corresponding 95% confidence intervals are
276 depicted as dashed red lines

277
278 Figure 4 shows that the precision gets poorer with increasing time-lags since the
279 autocorrelation function is then based on less data. We can also see time-correlation estimates with
280 a periodic behavior that differ significantly from zero for the short baseline setups, which indicates
281 that multipath might be present. The short-baseline patch-antenna setup (top) experiences time-
282 correlation estimates that take several hundreds of seconds to reach about zero, with a reduction
283 in time to reach zero when the Zephyr-antenna is used (bottom). These decorrelaton times are
284 similar to the phase-multipath time-correlation results found in Ray and Cannon (1999), Miller et
285 al. (2012), and Pesyna et al. (2014). However the zero-baseline time-correlation estimates in black
286 color, without multipath, fall reasonably well within the 95% CI and quickly drop to about zero
287 after a time-lag of one second. This can also be seen in the zoom-in depicted in Figure 5.

288

289 Time-correlation when reducing multipath
290 We will now further compare the zero-baseline results, based on independent data, to the short
291 baselines that were likely influenced by multipath effects (Figure 4). We will attempt to reduce
292 multipath for the short baselines by performing day-differences on the estimated positions while
293 taking into account the satellite repeatability period of approximately 23 h and 56 min, similar
294 to the DD residuals used to compute the code and phase STDs in Table 1.

295   Figure 5 depicts the autocorrelation functions for instantaneous short-baseline ambiguity-
296   fixed (left) and ambiguity-float (right) North/East/Up positioning, for the ublox+patch (top three
297   rows) and ublox+Zephyr (bottom three rows) models based on 1 h (1 s) of data. The
298   corresponding estimates based on ublox+patch zero-baseline data is depicted in black color. This
299   is given together with the 95% confidence interval (CI) for the autocorrelation function. A zoom-
300   in is used to depict the first five minutes (300 s) and 30 s only.

301   Figure 5 shows the overall larger time-correlation estimates for the short-baseline patch
302   antenna model over the 300 s in comparison to the Zephyr antenna. There is a relatively similar
303   magnitude of time-correlation estimates for the zero-baseline (black color) and the day-differenced
304   short-baseline (cyan) positioning time-series between the Zephyr and patch antenna (shown at
305   bottom three rows), particularly after a time-lag of about 10 s. The differences to the zero-baseline
306   are however larger when the patch antenna model is used for the short-baseline (top), which is
307   likely due to larger magnitudes of residual multipath that remain in the day-differenced positioning
308   solutions. Most importantly the zero-baseline L1+B1 phase-driven instantaneous ambiguity-fixed
309   positioning shows time-correlation estimates that drop down close to zero after a time-lag of one
310   second. The code-driven ambiguity-float positioning, however, shows time-correlation
311   coefficients for time-lags up to a few seconds that exceed values of about 0.2 (Table 3). This can,
312   for instance, be caused by receiver-related filtering to bring down the code observation noise level,
313   see also Bona (2000) and Li et al. (2008; 2016).

314   Table 3 summarizes the zero-baseline time-correlation estimates for different time lags
315   between $\tau = 0, ... ,4$ s, where the Trimble NetRS L1+L2 GPS time-correlation estimates are based
316   on day-differenced short-baseline data. In support of Table 3, Figure 6 shows the corresponding
317   survey-grade Trimble NetRS receiver L1+L2 GPS results. For both L1 and L2 code and phase one
318   can see that the time-correlation drops down to close to zero after one second for the day-
319   differenced positions, where multipath has been largely reduced.

320
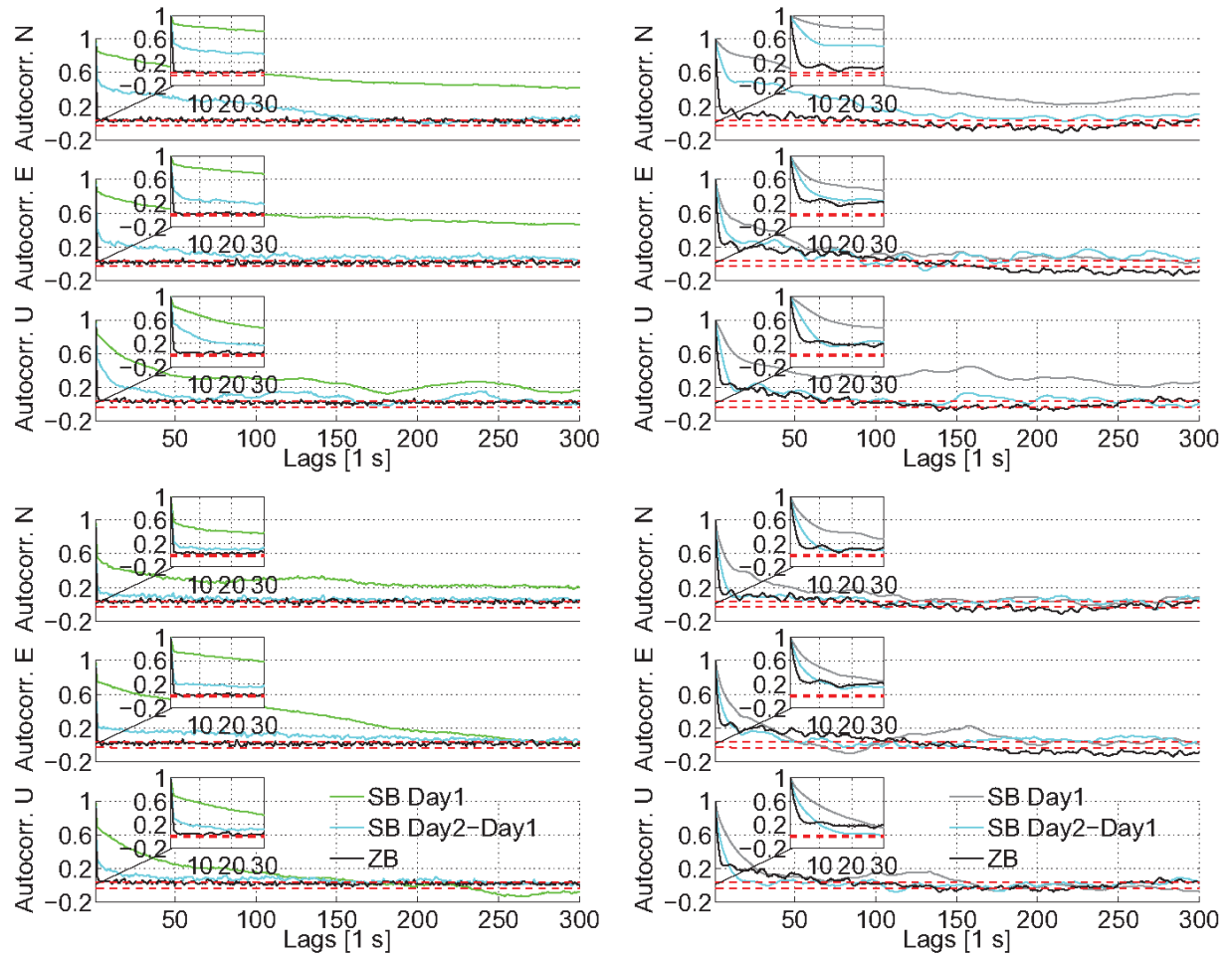
Fig. 5 Autocorrelation coefficients for L1+B1 GPS+BDS instantaneous short-baseline ambiguity-fixed (left) and ambiguity-float (right) positioning errors based on 1 h (1 s). Day1 is Jan 5, at 02:50 (hh:mm) UTC for patch in the top three rows and Jan 8, 2016 at 02:38 (hh:mm) UTC for Zephyr in bottom three rows. The corresponding autocorrelation coefficients for day-differenced, Jan 6 - Jan 5 for patch and Jan 9 - Jan 8 for Zephyr, and zero-baseline, ublox+patch at Apr 15 of 2016 at 19:39 (hh:mm) UTC, positioning are also shown. Their corresponding 95% confidence intervals are depicted as dashed red lines. A zoom-in is given for the first 300 s and 30 s, respectively

Table 3 Time-correlation estimates ($\hat{\rho}_\tau$) for different time lags $\tau = 0, \dots, 4$ s of the day-differenced N/E/U ambiguity-float short-baseline (day-differenced) positioning for Trimble NetRS L1+L2 GPS, and zero-baseline for the L1+B1 GPS+BDS ublox receivers with patch antennas. Ambiguity-fixed solutions are shown within parentheses. All depicted results are from Figures 5 and 6

Receiver/antenna and model	Positioning	Time lag	Autocorrelation coefficient $\hat{\rho}_\tau$		
			N	E	U
Ublox+patch	Float (fixed)	$\tau = 0$ (s)	1.000 (1.000)	1.000 (1.000)	1.000 (1.000)
L1+B1 GPS+BDS	Float (fixed)	$\tau = 1$ (s)	0.634 (0.055)	0.592 (0.055)	0.646 (0.107)
(zero-baseline)	Float (fixed)	$\tau = 2$ (s)	0.409 (0.022)	0.322 (0.043)	0.446 (0.056)
	Float (fixed)	$\tau = 3$ (s)	0.278 (0.019)	0.176 (0.039)	0.311 (0.035)
	Float (fixed)	$\tau = 4$ (s)	0.245 (-0.017)	0.137 (0.025)	0.254 (0.047)
Trimble	Float (fixed)	$\tau = 0$ (s)	1.000 (1.000)	1.000 (1.000)	1.000 (1.000)
NetRS+Zephyr	Float (fixed)	$\tau = 1$ (s)	0.131 (0.073)	0.236 (0.089)	0.125 (0.081)
L1+L2 GPS	Float (fixed)	$\tau = 2$ (s)	0.114 (0.015)	0.173 (0.037)	0.065 (0.093)
(day-differenced	Float (fixed)	$\tau = 3$ (s)	0.063 (0.008)	0.129 (0.014)	0.075 (0.066)
short-baseline)	Float (fixed)	$\tau = 4$ (s)	0.047 (-0.011)	0.089 (0.018)	0.035 (0.066)
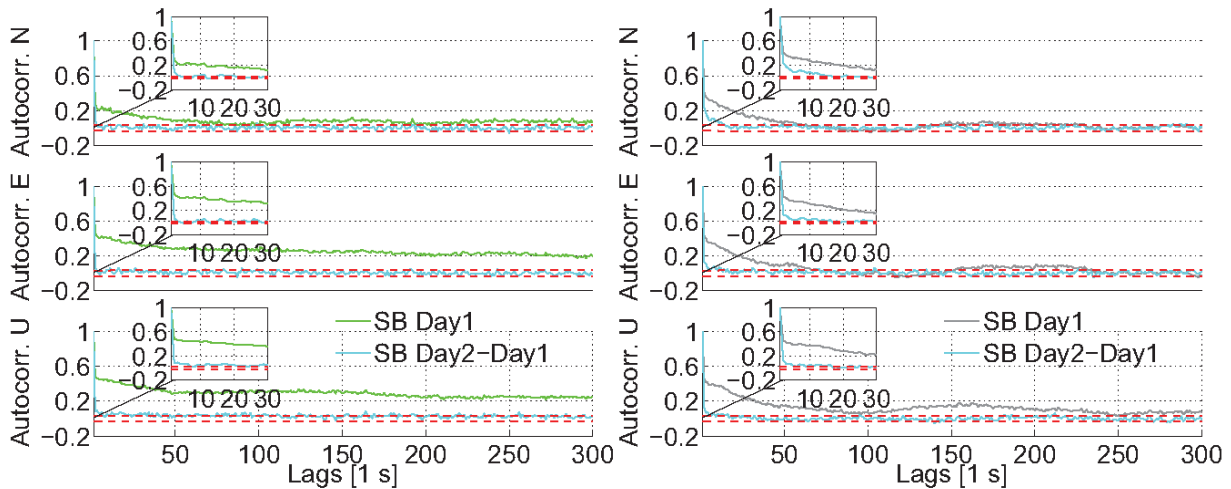
Fig. 6 Autocorrelation coefficients for Trimble NetRS+Zephyr L1+L2 GPS instantaneous short-baseline ambiguity-fixed (left) and ambiguity-float (*right*) positioning errors, based 1 h (1 s). Day1 is Jan 8, 2016 at 02:38 (hh:mm) UTC. The corresponding autocorrelation coefficients for day-differenced (Jan 9 - Jan 8, 2016) positioning is also shown. Their corresponding 95% confidence intervals are depicted as dashed red lines. A zoom-in window is given for the first 300 s and 30 s, respectively

351 **Low-cost RTK positioning**

352 We are now in the position to test our (co)variances that were estimated by LS-VCE. For this

353 purpose, we will use data that is independent of data used to estimate the STDs in Tables 1-2. The

354 positioning stochastic models will be based on STDs estimated from 2 h (1 s) data for the Zephyr

355 antenna models, whereas for the patch antenna model a 24 h period is used so that any multipath

356 effects are more likely to average out over time (Table 1). In the evaluations we neglect the cross-

357 correlation coefficients. To avoid the earlier-referenced receiver-induced time-correlation a 30 s

358 measurement interval will also be used.

359

360 Positioning performance

361 The instantaneous RTK positioning results for 24 h data are shown in Figure 7. The 95%

362 empirical and formal confidence ellipse and interval are shown in green and red, respectively.

363 They were computed from the empirical and formal position variance matrices. The empirical

364 variance matrix was estimated from the positioning errors as obtained from comparing the

365 estimated positions to precise benchmark coordinates. The formal variance matrix used is

366 determined from the mean of all single-epoch formal variance-matrices.

367
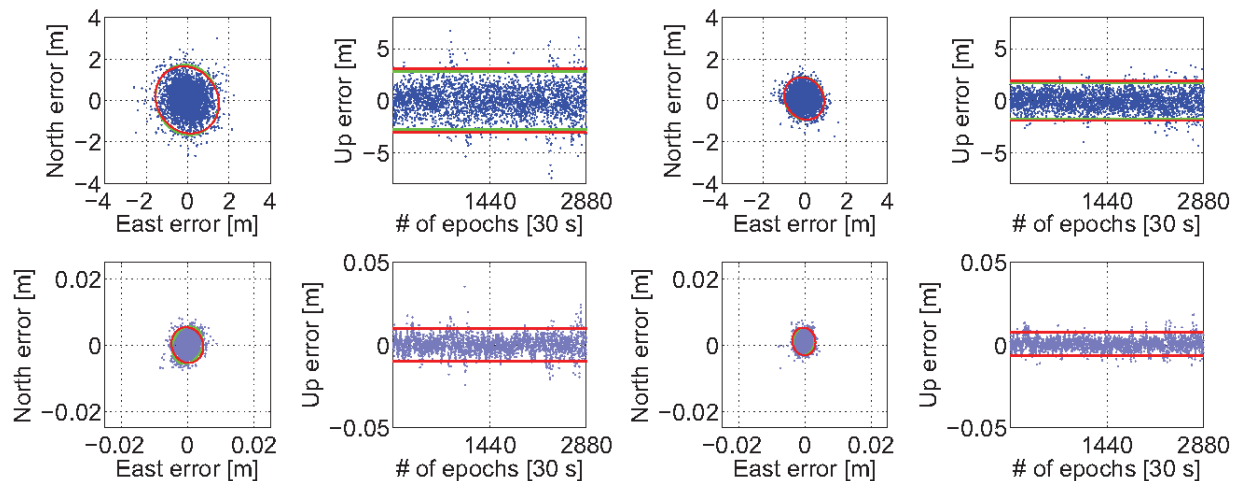
368
369 **Fig. 7** Few-meter baseline horizontal (N, E) position scatter and corresponding vertical (U) time

370 series of the float (top) and correctly fixed (bottom) L1+B1 GPS+BDS single-epoch RTK

371 solutions for an elevation cut-off angle of 10°. The 95% empirical and formal confidence ellipse

372 and interval is shown in green and red, respectively. The 24 h (30 s) period is 22:00-22:00 UTC

373 Jan 5-6 for patch in the left two columns and 21:48-21:48 (hh:mm) UTC Jan 8-9, 2016 for Zephyr

374 in the right two columns, which are periods independent of the periods used to determine the

375 stochastic model through the code/phase STDs in Table 2

376

377   Figure 7 shows a good fit between the formal and empirical confidence ellipses and

378 intervals, which thus illustrates realistic LS-VCE STDs in Table 2 that were used in the stochastic

379 model. Note, the improvement by two orders of magnitude when going from float to fixed

380 solutions, and that the ublox+Zephyr antenna model has significantly more precise ambiguity-float

381 positioning solutions in comparison to when patch antennas are used.

382

383 Ambiguity resolution and positioning performance for higher cut-off angles

384 We will investigate the low-cost L1+B1 GPS+BDS positioning performance for high elevation

385 cut-off angles to mimic situations in urban canyon environments or when low-elevation multipath

386 is to be avoided. Comparisons will be made to the survey-grade Trimble NetRS L1+L2 GPS

387 receivers. In Teunissen et al. (2014) and Odolinski and Teunissen (2016) it was shown that a good

388 ambiguity resolution performance does not necessarily imply a good positioning performance,

389 hence we will also investigate what effect this will have on our models at hand.

390   To investigate the ambiguity resolution performance, we consider the ambiguity success-

391 rates (SRs). We can make use of the SR formula of Teunissen (1998),

392 $$P[\check{z}_{IB} = z] = \prod_{i=1}^{n} \left[2\Phi\left(\frac{1}{2\sigma_{\hat{z}_{i|I}}} \right) - 1 \right] \qquad (9)$$

393 where $P[\check{z}_{IB} = z]$ denotes the probability of correct integer estimation of the integer bootstrapped

394 (IB) estimator $\check{z}_{IB}$ and $\sigma_{\hat{z}_{i|I}}$, $i = 1, ..., n$, $I = \{1, ..., (i - 1)\}$, denote the conditional STDs of the

395 LAMBDA decorrelated ambiguities. The bootstrapped SR (9) is easy to compute and is also a

396 sharp lower bound of the integer least-squares (ILS) SR (Teunissen 1999).

397   Figure 8 depicts the single-epoch SRs of the two RTK models over two days of data. The

398 SRs are computed based on epochs with the condition of Positional Dilution of Precision (PDOP)

399 ≤ 10 and averaged over all epochs. By including and excluding epochs with large PDOPs, we

400 will show how the positioning performance of the different models are affected by poor receiver-

satellite geometries. The results reveal that the L1+B1 ublox+Zephyr (full black lines) has similar PDOP-conditioned formal ambiguity SRs for cut-off angles up to 25° when compared to the Trimble NetRS L1+L2 GPS model (blue lines). The L1+B1 ublox+patch model (dotted black lines) has also a similar performance to the two other models for a cut-off angle of 10°, whereas the performance gets worse with increasing cut-off angles.
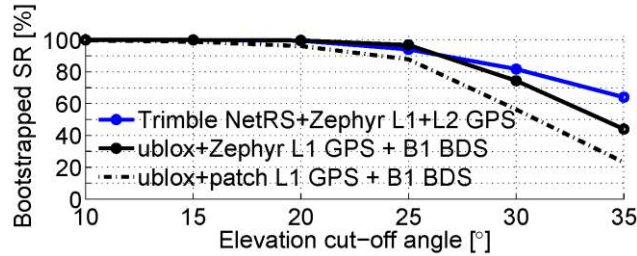
Fig. 8 Single-epoch bootstrapped (BS) success-rate (SR) for L1 + L2 GPS and L1 + B1 GPS+BDS, as function of the elevation cut-off angle. The results are based on data in Jan 4-6 and Jan 6-8, 2016 for the patch and Zephyr antenna models, respectively. The BS SRs are taken as a mean of all single-epoch SRs over two days, and conditioned on PDOP≤ 10

The formal results in Figure 8 are very promising. Hence in the next step, we will investigate the corresponding empirical performance of the different models. To better understand how this exclusion of epochs with large PDOPs influence the empirical ambiguity-fixed and ambiguity-float positioning performance, Table 4 shows the corresponding positioning STDs for two days of data. These STDs were computed by comparing the estimated positions to very precise benchmarks. In addition to the positioning performance we depict in Table 4 the corresponding empirical ILS SRs for full ambiguity-resolution, which is given by,

$$P_{S_E} = \frac{\text{\# of correctly fixed epochs}}{\text{total \# of epochs}} \tag{10}$$

In addition and within parentheses the corresponding bootstrapped SRs are given.

Table 4 shows that all PDOP-conditioned ILS SRs are consistent with the BS SRs, which again shows that the STDs in Table 2 used for the stochastic models are realistic. It also shows that the L1+B1 ublox+patch model has, as expected, smaller SRs in comparison to when the survey-grade Zephyr antenna is used. Moreover, this latter ublox+Zephyr model has comparable SRs to the PDOP-conditioned SRs of the Trimble NetRS L1+L2 GPS model for cut-off angles up

to 25°, similar to what we showed in the previous formal analysis (Figure 8).

Table 4 Single-epoch empirical STDs (N, E, U) of correctly ambiguity-fixed positions for Trimble NetRS L1+L2 GPS, L1+B1 ublox+Zephyr and ublox+patch, respectively, together with their ILS SR, for $20° - 35°$ elevation cut-off and 48 hours of data in Jan 4-6 and Jan 6-8 2016, respectively. The empirical STDs and ILS SRs are also shown when conditioned on PDOP≤10, and bootstrapped SRs are shown within parentheses

| Model	Empirical STDs [mm], ILS SR (%)															
Cut-off (◦):	20				25				30				35			
	N	E	U	SR	N	E	U	SR	N	E	U	SR	N	E	U	SR
L1+L2 Trimble NetRS	3	2	7	99.9 (99.9)	90	23	114	99.4 (99.3)	73	27	195	93.0 (92.9)	75	37	229	80.2 (80.2)
PDOP≤ 10	3	2	6	99.5 (99.5)	3	3	8	94.1 (94.0)	4	3	9	81.8 (81.7)	5	3	11	64.1 (64.0)
L1+B1 ublox+Zephyr	2	1	4	99.8 (99.7)	2	2	5	97.8 (96.8)	2	2	6	77.3 (74.7)	2	2	7	50.3 (45.0)
PDOP≤ 10									2	2	6	76.7 (74.4)	2	2	6	48.8 (44.0)
L1+B1 ublox+patch	2	2	6	96.9 (96.1)	3	2	7	89.8 (87.8)	3	2	8	57.3 (56.4)	3	4	12	25.0 (23.2)
PDOP≤ 10									3	2	8	57.0 (56.3)	3	3	10	24.9 (23.1)

In support of a better understanding Table 4, Figures 9-10 shows typical positioning examples of the different models for an elevation cut-off angle of 10° and 25°, respectively. The first row shows the local horizontal (N, E) positioning scatterplots and the second row the vertical (U) time series over two days of data. The float solutions are depicted in gray, incorrectly and correctly fixed solutions in red and green, respectively. The zoomed-in is given to better show the spread of the correctly fixed solutions with millimeter-centimeter level precisions. The formal ambiguity-float STDs are also shown under the Up time series as to reflect consistency between the empirical and formal positioning results. In addition, we depict in Figure 9 the Ambiguity Dilution of Precision (ADOP) as introduced by Teunissen (1997), as an easy-to-compute scalar diagnostic to measure the intrinsic model strength for successful ambiguity resolution. The ADOP

451   is defined as

452    $$ADOP = \sqrt{|Q_{\hat{a}\hat{a}}|^{\frac{1}{n}}} \qquad \text{(cycle)} \tag{11}$$

453   with n the dimension of the ambiguity vector, $Q_{\hat{a}\hat{a}}$ is the ambiguity variance matrix, and $|.|$

454   denotes the determinant. ADOP gives a good approximation to the average precision of the

455   ambiguities, and it also provides for a good approximation to the ILS SR (Verhagen 2005). The

456   rule-of-thumb is that an ADOP smaller than about 0.12 cycles corresponds to an ambiguity SR

457   larger than 99.9% (Odijk and Teunissen 2008).
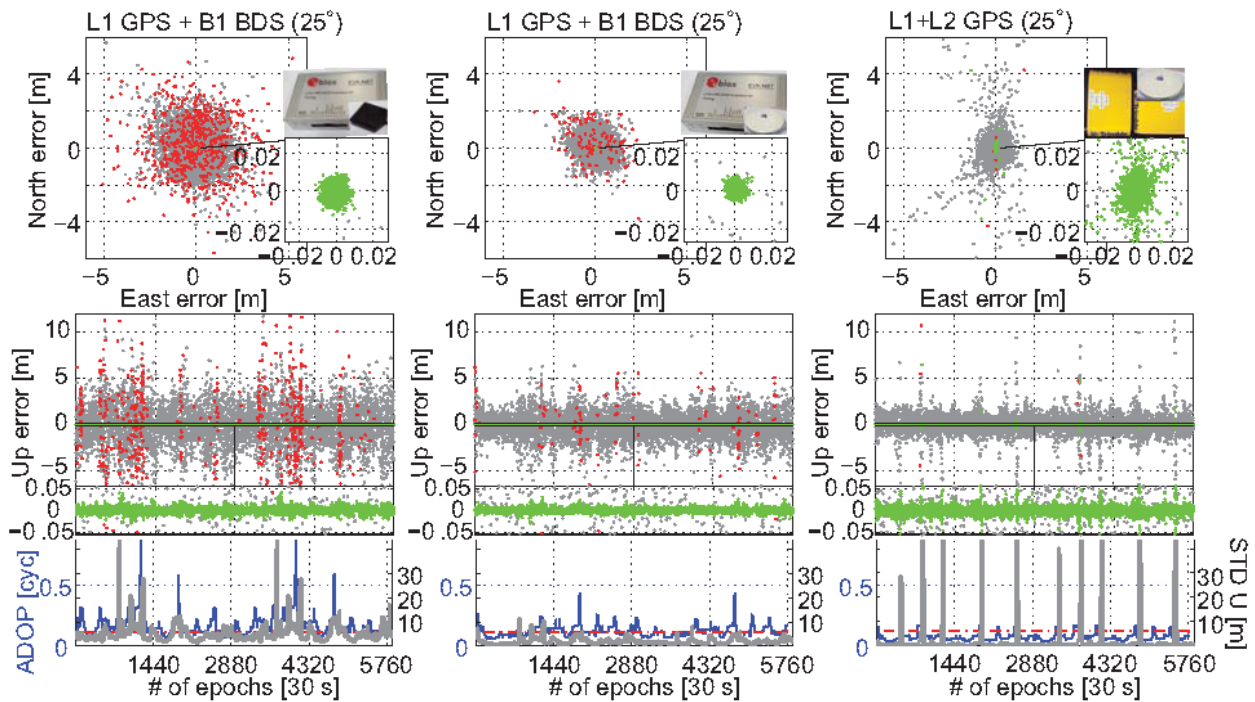
458
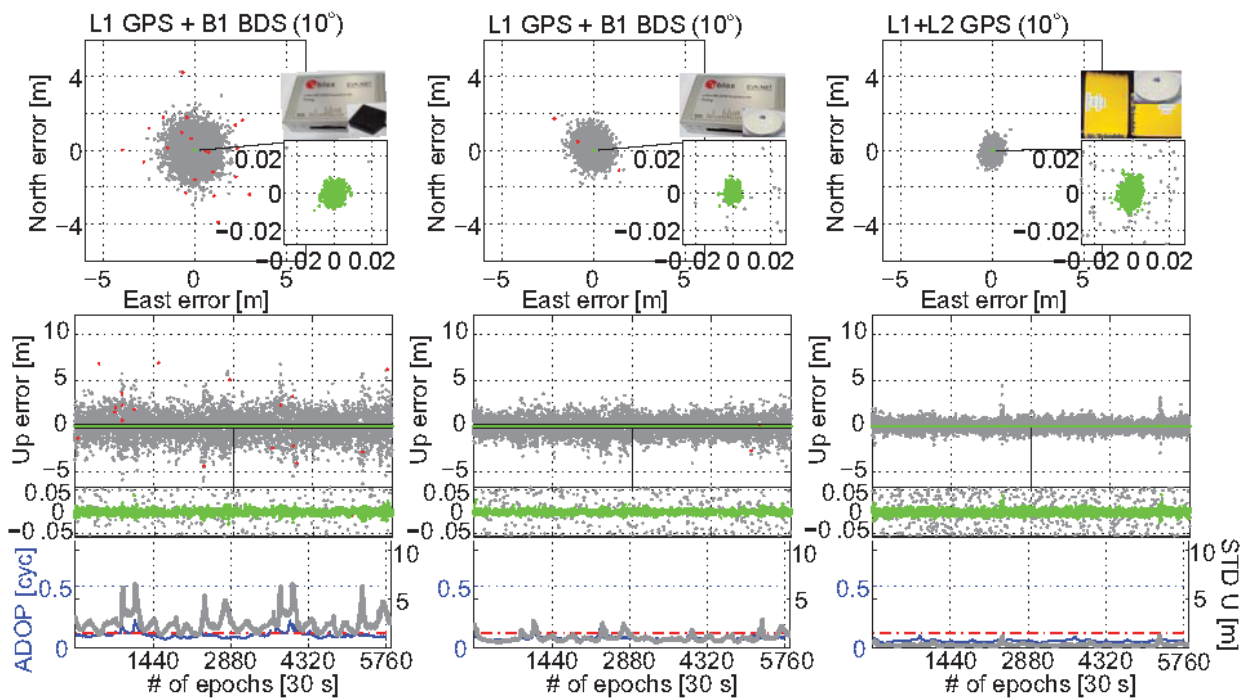
459

460   **Fig. 9** Few-meter baseline horizontal (N, E) scatterplots and vertical (U) time series for L1 + B1

461   ublox+patch (first column) with 99.5% ILS SR, L1 + B1 ublox+Zephyr (second column) with

462   100% ILS SR, and Trimble L1+L2 GPS (third column) with 100% ILS SR, using 10° cut-off.

463   The results are based on data in Jan 4-6 for ublox+patch and Jan 7-8, 2016 for

464   ublox/Trimble+Zephyr. The SRs are conditioned on PDOP≤ 10 and computed based on all

465   epochs. The correctly fixed solutions are depicted in green, incorrectly fixed in red, and ambiguity-

466   float in gray. Below the vertical time series the ADOP is depicted in blue color, the 0.12 cycles

467   level as red, and ambiguity-float Up formal STDs are shown in gray

468

469   Figures 9-10 reveal that more solutions are likely to be incorrectly fixed (red dots) when
470   the ADOPs (blue lines) are larger than the 0.12 cycle level (red dashed lines). Figure 9 also shows
471   that the L1+B1 ublox+patch model achieves an ILS SR similar to that of the survey-grade L1+L2
472   GPS model for the cut-off angle of 10°. The SR is namely 99.5% for the L1+B1 ublox+patch
473   model and 100% for the L1+L2 GPS model. This ILS SR corresponds to the availability of
474   correctly fixed solutions (green dots) with millimeter to centimeter level positioning precision over
475   the two days.

476

477

478 **Fig. 10** Few-meter baseline horizontal (N, E) scatterplots and vertical (U) time series for L1 + B1
479   ublox+patch (first column) with 89.8% ILS SR, L1 + B1 ublox+Zephyr (second column) with
480   97.8% ILS SR, and Trimble L1+L2 GPS (third column) with 94.1% ILS SR, using 25° cut-off.
481   The results are based on data in Jan 4-6 for ublox+patch and Jan 7-8, 2016 for
482   ublox/Trimble+Zephyr. The SRs are conditioned on PDOP $\leq$ 10 and computed based on all
483   epochs. The correctly fixed solutions are depicted in green, incorrectly fixed in red, and ambiguity-
484   float in gray. Below the vertical time-series the ADOP is depicted in blue color, the 0.12 cycles
485   level as red, and ambiguity-float Up formal STDs are shown in gray

486

487   Figure 10 shows that the L1+B1 ublox patch antenna model has some instances with

significantly different ADOPs in comparison to the corresponding Zephyr antenna model for the cut-off angle of $25°$, for example just before epochs 1440 and 4320, respectively. This is mainly because the two models are based on different days of data where the BDS MEO satellite constellation does not repeat each day and thus the patch antenna model has a smaller number of satellites for some epochs that result in larger ADOPs. The L1+L2 GPS model has moreover large ambiguity-fixed positioning excursions at the same time as the formal STDs are large for the cut-off angle of $25°$, due the poor GPS-only receiver-satellite geometry for this high cut-off angle. This is also reflected by the corresponding relatively large ambiguity-fixed STDs depicted in Table 4 that are improved from decimeter- to millimeter-level when the PDOP≤10 condition is applied. Finally, Figure 10 shows that L1+B1 ublox+Zephyr has a larger SR of 97.8% when compared to the PDOP-conditioned SR for L1+L2 GPS of 94.1% for the cut-off angle of $25°$ (Table 4), owing to the use of BDS that improves the receiver-satellite geometry.

Low-cost RTK positioning for a 7 km baseline

So far we have considered baseline lengths of a few meters only. One might wonder whether the low-cost L1+B1 GPS+BDS ublox RTK solution would perform similarly well for baselines where small residual ionospheric delays are present. Hence in the following we analyze the RTK positioning performance for a 7 km baseline in Dunedin for 24 h (30 s) during Jan 18-19, 2016 (Figure 1). The Australian Space Forecast centre (http://www.sws.bom.gov.au/Geophysical/2/1) warned for an increased geomagnetic disturbance during this period, which implies that residual ionospheric delays can indeed be present. We make use of the same stochastic model settings as in the previous Section (Table 2), which is based on an independent baseline.

To deal with any residual ionospheric delays we also add to our model (1) a vector with slant ionosphere pseudo-observations $\iota = [\iota_G^T, \iota_B^T]^T \in \mathbb{R}^{s_G + s_B}$ and parameterize the ionospheric delays. The inclusions of these pseudo-observables can provide us with stochastic information of the ionospheric delays between stations, which is also referred to as the "ionosphere-weighted" model. The stochastic model settings of these observables are set by following the rule of thumb by Schaffrin and Bock (1988), where the double-differenced (DD) slant ionospheric delay zenith-referenced STD can be modeled as a function of the baseline length as 1.4 mm/km. For a baseline length of 7 km this corresponds to a DD STD of almost 10 mm.

518   As to verify whether slant ionospheric delays are indeed present, we depict in Figure 11

519   the DD slant ionospheric delays with the ionosphere-weighted stochastic model settings mentioned

520   above, while making use of a L1+B1 ublox+Zephyr geometry-fixed and ambiguity-fixed model.

521   The DD slant ionospheric delays are shown for all satellites (GPS+BDS) with an elevation cut-off

522   angle of 20°, as to avoid any low-elevation multipath on our estimates. At top of Figure 11 the

523   few-meter baseline setup is shown to illustrate the situation when ionospheric delays are not

524   present, whereas at bottom the corresponding 7 km baseline results are depicted.

525

526
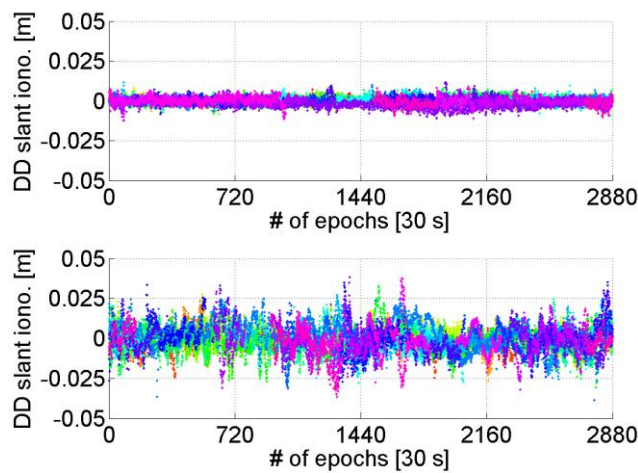
527

528   **Fig. 11** DD ambiguity-fixed slant ionospheric delays using L1+B1 GPS+BDS ublox+Zephyr for

529   a few meter baseline (top) on Jan 7 and seven kilometer baseline (bottom) on Jan 18, 2016 for an

530   elevation cut-off angle of 20°. The ionosphere-weighted model has been used with the DD slant

531   ionospheric delay zenith-referenced STD set to approximately 10 mm for both models

532

533   Figure 11 shows, as expected, that the magnitudes of the slant ionospheric delays for the

534   few-meter baseline resemble that of the phase noise precision (Figure 3). The 7 km baseline,

535   however, show significantly larger magnitudes of the slant ionospheric delays that exceeds the

536   phase noise precision, which indicates that the slant ionospheric delays should indeed be modeled.

537   To investigate whether the stochastic model settings as determined from a few meter

538   baseline is also applicable to the 7 km baseline, we show in Figure 12 the corresponding

539   instantaneous RTK positioning results for ublox+Zephyr L1+B1 GPS+BDS and Trimble

540   NetRS+Zephyr L1+L2 GPS, while making use of an elevation cut-off angle of 10°. There is a

541   good fit between the formal and empirical positioning confidence ellipses and intervals, which

542 thus again illustrates realistic LS-VCE STDs in Table 2 that were used in the stochastic model.

543 This in addition to the STD used for the DD slant ionosphere pseudo-observations.

544
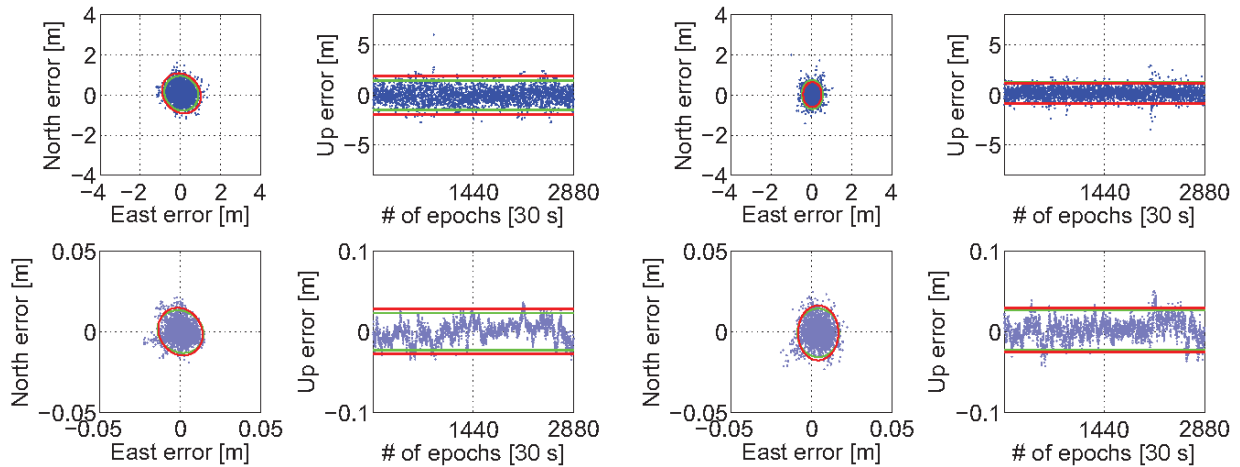
545
546 **Fig. 12** Seven kilometer baseline horizontal (N, E) position scatter and corresponding vertical (U)

547 time-series of the float (top) and correctly fixed (bottom) L1+B1 GPS+BDS (left two columns)

548 and L1+L2 GPS (right two columns) single-epoch RTK solutions for an elevation cut-off angle of

549 10˚. The 95% empirical and formal confidence ellipse and interval is shown in green and red,

550 respectively. The 24 h (30 s) period is 23:0-23:00 UTC Jan 18-19, 2016, where the baseline is

551 independent of the few meter baseline used to determine the stochastic model through the

552 code/phase STDs in Table 2

553
554   Figure 13 depicts the corresponding float, incorrectly and correctly fixed positioning

555 solutions at top, respectively, together with the ADOPs and ambiguity-float Up formal STDs at

556 the bottom. The figure reveals that the L1+B1 GPS+BDS model has some instances around and

557 after epoch 720 when the ADOP (blue color) is relatively large which consequently yields

558 incorrectly fixed solutions (red). The instantaneous ILS SR for the L1+B1 ublox+Zephyr model is

559 97%, whereas the corresponding ILS SR for the Trimble NetRS L1+L2 model is 99.8%. We have

560 thus illustrated that the low-cost receiver-solution still has the potential to perform very well even

561 for a baseline length of 7 km, where small residual ionospheric delays are present.

562
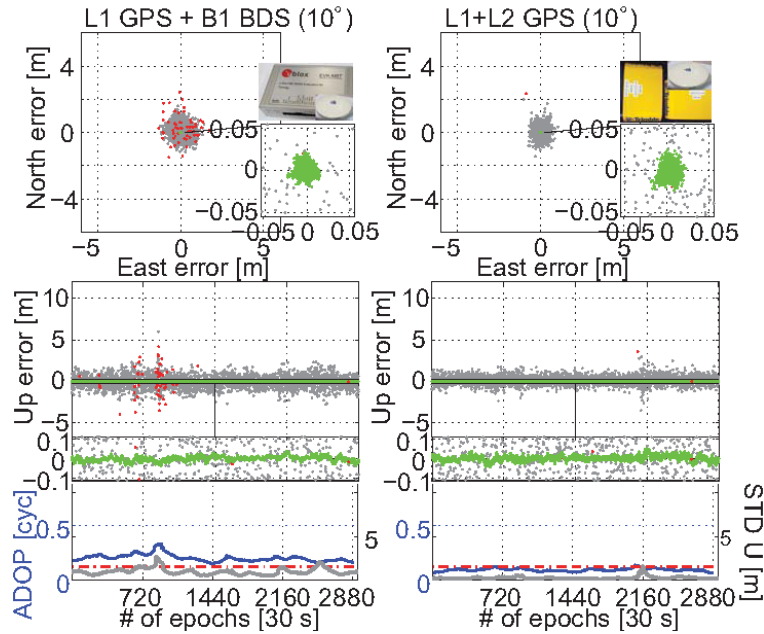
Fig. 13 Seven kilometer baseline horizontal (N, E) scatterplots and vertical (U) time series for L1 + B1 ublox+Zephyr (first column) with 97.0% ILS SR, and Trimble L1+L2 GPS (second column) with 99.8% ILS SR, using 10° cut-off during Jan 18-19, 2016. The correctly fixed solutions are depicted in green, incorrectly fixed in red, and ambiguity-float in gray. Below the vertical time series the ADOP is depicted in blue color, the 0.12 cycles level as red, and ambiguity-float Up formal STDs are shown in gray

Conclusions

We evaluated a low-cost ublox L1+B1 GPS+BDS RTK model and compared its ambiguity resolution and positioning performance to a survey-grade receiver L1+L2 GPS solution, in Dunedin, New Zealand. The least-squares variance component estimation (LS-VCE) procedure was initially used to determine the (co)variances of the low-cost receivers. The estimated (co)variances are needed so as to formulate a realistic stochastic model. Otherwise the ambiguity resolution performance and hence the achievable positioning precisions would deteriorate. For the same reasons, we also investigated the presence of receiver-induced time-correlation. Since we analyzed a short baseline, the LS-VCE and time-correlation estimates were shown to likely be affected by multipath. To mitigate multipath we connected the low-cost receivers to survey-grade antennas and compared the performance to a zero-baseline setup.

    It was shown that the survey-grade antennas can significantly improve the performance for

the low-cost receivers so that the code and phase noise estimates more resemble that of survey-grade receivers. The cross-correlations between GPS L1 code and phase and BDS B1 code and phase were all shown to be close to zero for the low-cost receivers at hand, whereas significant cross-correlation was present for the L1 and L2 phase observables of the survey-grade receivers. The receiver-induced time correlation was also shown to be close to zero for phase in both receiver types, whereas some time-correlation existed for the code observables in the low-cost receivers. The LS-VCE STDs were shown to be realistically estimated for both an independent period and baseline. We also demonstrated that the low-cost receivers, which cost a few hundred USDs, can give competitive instantaneous ambiguity resolution and positioning performance to the survey-grade receivers, which cost several thousand USDs. This was shown both formally and empirically, and is particularly true when the low-cost receivers are connected to survey-grade antennas. It was finally shown that the low-cost receiver-solution with survey-grade antennas still has the potential to achieve competitive ambiguity resolution and positioning performance to the survey-grade receiver solution for a baseline length of 7 km, where small residual slant ionospheric delays are present.

References

Amiri-Simkooei AR, Tiberius CCJM (2007) Assessing receiver noise using GPS short baseline time series. GPS Solut 11(1):21–35

Amiri-Simkooei AR, Teunissen PJG, Tiberius CCJM (2009) Application of Least-Squares Variance Component Estimation to GPS observables. Journal of Surveying Engineering 135(4):149–160

Amiri-Simkooei AR, Jazaeri S, Zangeneh-Nejad F, Asgari J (2016) Role of stochastic model on GPS integer ambiguity resolution success rate. GPS Solut 20(1):51–61

Axelrad P, Larson K, Jones B (2005) Use of the correct satellite repeat period to characterize and reduce site-specific multipath errors. Proc. ION ITM 2005, Institute of Navigation, Long Beach, CA, September 13-16, 2638 - 2648

Bona P, Tiberius CCJM (2000) An experimental assessment of observation cross-correlation in dual frequency receivers. Proc. ION GPS 2000, Institute of Navigation, Salt Lake City, UT, September 19-22, 792 - 798

Bona P (2000) Precision, cross correlation, and time correlation of GPS phase and code observations. GPS Solut 4(2);3–13

Euler HJ, Goad C (1991) On optimal filtering of GPS dual frequency observations without using orbit information. Bull Geod 65(2):130–143

He H, Li J, Yang Y, Xu J, Guo H, Wang A (2014) Performance assessment of single- and dual-frequency BeiDou/GPS single-epoch kinematic positioning. GPS Solut 18(3):393–403, doi:10.1007/s10291-013-0339-3

Jiang Y, Yang S, Zhang G, Li G (2011) Coverage performance analysis on combined-GEO-IGSO satellite constellation. Journal of electronics 28(2):228–234

Li B, Shen Y, XU P (2008) Assessment of stochastic models for GPS measurements with different types of receivers. Chi Sci Bull 53(20):3219–3225

Li B (2016) Stochastic modeling of triple-frequency BeiDou signals: estimation, assessment and impact analysis. J Geod 90(7):593–610

Miller C, O'Keefe K, Gao Y (2012) Time Correlation in GNSS Positioning over Short Baselines. J Surveying Engineering 138(1):17–24

Mongredien C, Doyen JP, Strom M, Ammann D (2016) Centimeter-Level Positioning for UAVs and Other Mass-Market Applications. Proc. ION GNSS 2016, Institute of Navigation, Portland, Oregon, September 12-16, 1441 - 1454

Montenbruck O, Hauschild A, Steigenberger P, Hugentobler U, Teunissen PJG, Nakamura S (2013) Initial assessment of the COMPASS/BeiDou-2 regional navigation satellite system. GPS Solut 17(2):211-222 doi:10.1007/s10291-012-0272-x

Nadarajah N, Teunissen PJG, Raziq N (2013) BeiDou Inter-Satellite-Type Bias Evaluation and Calibration for Mixed Receiver Attitude Determination. Sensors 13(7):9435–9463

Odijk D, Teunissen PJG (2008) ADOP in closed form for a hierarchy of multi-frequency single-baseline GNSS models. J Geod 82:473-492

Odolinski R, Teunissen PJG (2016) Single-Frequency, Dual-GNSS versus Dual-Frequency, Single-GNSS: A Low-cost and High-grade receivers GPS-BDS RTK analysis. J Geod doi:10.1007/s00190-016-0921-x

Odolinski R, Teunissen PJG, Odijk D (2015) Combined BDS, Galileo, QZSS and GPS single-frequency RTK. GPS Solut 19(1):151–163, doi:10.1007/s10291-014-0376-6

Pesyna KM, Heath R, Humphreys TE (2014) Centimeter Positioning with a Smartphone-Quality GNSS Antenna. Proc. ION GNSS 2014, Institute of

657   Navigation, Tampa, FL, September 8-12, 1568 - 1577

658 Ray J, Cannon M (1999) Characterization of GPS carrier phase multipath. Proc. ION NTM 1999,
659   San Diego, CA, January 25-27, 343 - 352

660 Schaffrin B, Bock Y (1988) A unified scheme for processing GPS dual-band phase observations.
661   Bull Geod 62:142–160

662 Takasu T, Yasuda A (2008) Evaluation of RTK-GPS Performance with Low-cost Single-
663   frequency GPS Receivers. In: International Symposium on
664   GPS/GNSS 2008, Odaiba, Tokyo, November 11-14, 852–861

665 Takasu T, Yasuda A (2009) Development of the low-cost RTK-GPS receiver with an open
666   source program package RTKLIB. In: International
667   Symposium on GPS/GNSS 2009, Jeju, Korea, November 4-6,
668   1 - 6

669 Teunissen PJG, Amiri-Simkooei AR (2008) Least-squares variance component estimation. J
670   Geod 82(2):65–82

671 Teunissen PJG, Tiberius CCJM, Jonkman JF, de Jong CD (1998) Consequences of the cross-
672   correlation measurement technique. In: Proceedings of
673   GNSS98, 2nd European symposium, Toulouse France,
674   October 20-23, pp 1–6

675 Teunissen PJG, Odolinski R, Odijk D (2014) Instantaneous BeiDou+GPS RTK positioning with
676   high cut-off elevation angles. J Geod 88(4):335–350

677 Teunissen PJG (1988) Towards a least-squares framework for adjusting and testing of both
678   functional and stochastic model. Internal research memo
679   Geodetic Computing Centre, Delft Reprint of original 1988
680   report (2004), No. 26

681 Teunissen PJG (1990) An integrity and quality control procedure for use in multi sensor
682   integration. In: Proceedings of the 3rd International
683   Technical Meeting of the Satelllite Division of the Institute of
684   Navigation (ION GPS 1990), Colorado Spring, CO, pp 513–
685   522, also published in: Volume VII of the GPS Red Book:
686   Integrated systems, ION Navigation, 2012.

687 Teunissen PJG (1995) The least squares ambiguity decorrelation adjustment: a method for fast
688   GPS integer estimation. J Geod 70(1):65-82

689 Teunissen PJG (1997) A canonical theory for short GPS baselines. Part I: The baseline precision,
690   Part II: The ambiguity precision and correlation, Part III: The
691   geometry of the ambiguity search space, Part IV: Precision
692   versus reliability. J Geod   71(6): 320-336, 71(7): 389-401,
693   71(8): 486-501, 71(9): 513-525

694 Teunissen PJG (1998) Success probability of integer GPS ambiguity rounding and bootstrapping.
695   J Geod 72(10):606–612

696 Teunissen PJG (1999) An optimality property of the integer least-squares estimator. J Geod
697   73(11):587–593

698   Verhagen S, Teunissen PJG, Odijk D (2012) The Future of Single-Frequency Integer Ambiguity
699   Resolution. In: N. Sneeuw et al. (eds.), VII Hotine-Marussi
700   Symposium on Mathematical Geodesy, International
701   Association of Geodesy Symposia 137,   doi:10.1007/978-3-
702   642-22078-4_5

703   Verhagen S (2005) On the reliability of integer ambiguity resolution. Navigation 52(2):99–110

704   Wang G, de Jong K, Zhao Q, Hu Z, Guo J (2015a) Multipath analysis of code measurements for
705   BeiDou geostationary satellites. GPS Solut 19(1):129–139,
706   doi: 10.1007/s10291-014-0374-8

707   Wang M, Chai H, Liu J, Zeng A (2015b) BDS relative static positioning over long baseline
708   improved by GEO multipath mitigation. Adv Space Res
709   57(3):782-793.   doi:10.1016/j.asr.2015.11.032

710   Wisniewski B, Bruniecki K, Moszynski M (2013) Evaluation of RTKLIB's Positioning Accuracy
711   Using low-cost GNSS Receiver and ASG-EUPOS. Int J on
712   Marine Navigation and Safety of Sea Transportation 7(1):79–
713   85

714   Zaminpardaz S, Teunissen PJG, Nadarajah N (2016) GLONASS CDMA L3 ambiguity
715   resolution and positioning. GPS Solut doi:10.1007/s10291-
716   016-0544-y
717
718

719   **Authors Biographies**

Robert Odolinski conducted his Ph.D. studies at Curtin University, Australia in 2011 to 2014. His research focus is next generation multi-GNSS integer ambiguity resolution enabled precise positioning. In 2015 Robert started his position as a Lecturer/Research Fellow in Geodesy/GNSS at the School of Surveying, University of Otago, New Zealand. He is a member of the Joint Study Group in Multi-GNSS theory and algorithms of the International Association of Geodesy (IAG).

726

727

Peter Teunissen is currently a Professor of geodesy and navigation, the Head of Curtin GNSS Research Centre, and the Science Director of the Cooperative Research Centre for Spatial Information, Curtin University. He is also with Department of Geoscience and Remote Sensing, Delft University, Delft, The Netherlands. His current research interests include multiple GNSSs and the modeling of next-generation GNSS for high-precision positioning, navigation, and timing applications.

735

736

737